Exploring dust growth in the episodic WCd system WR140

J. W. Eatson*, J. M. Pittard and S. Van Loo
School of Physics and Astronomy, University of Leeds, Woodhouse Lane, Leeds LS2 9JT, UK

ABSTRACT

Key words: stars: Wolf-Rayet – methods: numerical – binaries: general

1 INTRODUCTION

Dust formation in massive star binary systems is a particularly fascinating subject. Considering the immense photon fluxes and strong shocks involved, these systems should not form dust at all, and yet in some systems, all evidence points to the contrary. Colliding wind binary (CWB) systems were first hypothesised to explain highly luminous and variable x-ray emission in systems such as V444 Cyg and γ^2 Vel (Prilutskii & Usov 1976). These extremely bright emissions were found to be due to stellar wind collision with shock velocities of the order 10^3 km s^{-1}. The variability in x-ray emission can be explained if the phenomena occurs due to the orbit of a binary system, such as the Wind Collision Region (WCR) being occluded by the outflowing stellar winds and being occluded by the stars themselves. The system can also have an eccentric orbit, changing the shock strength as the orbital separation, $d_{\rm sep}$, varies. Despite this dust-hostile environment, CWB systems containing a Wolf-Rayet carbon phase star (WC) have been observed producing copious quantities of dust (so-called WCd systems). These systems typically convert around 1% of the stellar wind into dust a short time after wind collision; in more prolific systems such as WR104 up to 36% of the Wolf-Rayet (WR) outflow is converted into dust (Lau et al. 2020). This corresponds to dust production rates on the order of 10^{-6} M$_\odot$ yr^{-1}, rivalling other profuse dust producing phenomena such as AGB stars.

WCd systems can be sub-categorised further, into persistent, variable and episodic dust forming systems. Persistent systems, such as WR104 (Tuthill et al. 1999), produce dust at a constant rate, and as such produce extreme quantities of dust, as well as well-defined pinwheel patterns if the system is viewed face-on. Episodic systems, meanwhile, only produce dust for a limited period before entering a period of dormancy; this pattern is cyclical, and is predictably periodic. A good example of such an episodic system is WR140 (Williams et al. 1990), the subject of this paper. Variable systems have some characteristics of these two sub-types, having a distinct variability without a period of dust producing dormancy, such as WR98a (Monnier et al. 1999). Whether a system is persistent, variable or episodic is based on the system's orbital eccentricity. Highly eccentric systems appear to form episodic systems, with the "active" dust production period occurring immediately after periastron

passage, and a relatively short time thereafter. Meanwhile, persistent and variable systems have been observed to have more circular orbits, suggesting that the effect of a change in system separation distance, $d_{\rm sep}$, has a role in dust formation. The initial mechanism behind dust formation is not well understood. Whilst nascent amorphous carbon dust grain cores can condense within the photosphere of WC7-9 stars, these grain cores would be vaporised by the UV flux of both stars. However, within the WCR these grains appear to flourish. Observations of these systems show that infrared excess in wavelengths associated with amorphous grains is detected almost exclusively within the post-shock WCR (Soulain et al. 2018). Observations also indicate that dust formation occurs rapidly and close to the system, this requires strong radiative cooling for the immediate-post shock temperature to reduce from $\sim 10^7$ K to $\sim 10^4$ K (Williams et al. 1987, 1990). As such, dust formation appears to be encouraged in the WCR through a multitude of factors:

• Strong radiative cooling produces clumps of cool, high density gas where dust can rapidly grow.
• The high density of the post-shock WCR results in a high collision rate between carbon atoms and dust grains.
• The high density also shields nascent dust grains from the bulk of the UV emission from the stars.
• The rapid cooling in the immediate post-shock environment reduces gas-grain sputtering.

The dust formation can also be influenced by orbital separation, velocity shear and momentum ratio imbalance between the winds, producing variability on the timescale of a single orbit, or $t_{\rm dyn} \ll P$.

WCd systems are comparatively rare. Out of 106 confirmed WR binaries, only 9 are categorised as episodic WCd systems (Table 1). As these systems have a typical distance on the order of $1-10$ kpc, observation of WCds is difficult. Whilst these systems can be observed and the dusty WCR can be resolved, observation of the innermost, immediate post-shock dust forming region is not possible at this distance. As such, numerical simulation is necessary to determine dust formation in WCd systems. A contemporary example of such simulations is Hendrix et al. (2016), though the evolution of dust grains through cooling, growth and sputtering was not performed. In this paper we present a numerical simulation of the archetypical episodic WCd system WR140 with a co-moving dust model simulating grain growth and sputtering through gas-grain collisions. This simulation covers a temporal slice of the orbit of WR140 from phase $\Phi = 0.95$

	Persistent		Variable		Episodic	
	Total	Example	Total	Example	Total	Example
WC4	1	WR19	0	—	0	—
WC5	0	—	0	—	1	WR47C
WC6	1	WR124-10	0	—	0	—
WC7	3	WR102-22	0	—	4	WR140
WC8	6	WR13	1	WR48a	3	WR122-14
WC9	45	WR104	6	WR98a	1	WR75-11
Total	56		7		9	

Table 1. Number of WCd systems with a known spectral type and dust formation type from the Galactic Wolf Rayet Catalogue (Rosslowe & Crowther 2015). Systems with uncertain spectral types are not included, while systems labelled "d" are included within the "persistent" category for their associated spectral type.

to $\Phi = 1.10$, or the period immediately prior to and after periastron passage. We will discuss our methodology in Section 2, with a particular emphasis on our dust model in Subsection 2.2. Afterwards we will discuss the simulation and WR140 system parameters, as well as our data collection techniques in Section 3. Finally, we will discuss our results and conclude in Sections 4 and 5.

2 METHODOLOGY

The periodic dust forming system WR140 was simulated using a fork of the Athena++ hydrodynamical code (Stone et al. 2020). A series of modifications were implemented to simulate binary system orbits, stellar wind outflows and dust evolution. These simulations were conducted in 3D in a Cartesian co-ordinate system. The code solves a Riemann problem at each cell interface to determine the time-averaged values at the zone interfaces, and then solves the equations of hydrodynamics:

$$\frac{\partial \rho}{\partial t} + \nabla \cdot (\rho \boldsymbol{u}) = 0, \tag{1a}$$

$$\frac{\partial \rho \boldsymbol{u}}{\partial t} + \nabla \cdot (\rho \boldsymbol{u} \boldsymbol{u} + P) = 0, \tag{1b}$$

$$\frac{\partial \rho \varepsilon}{\partial t} + \nabla \cdot [\boldsymbol{u} (\rho \varepsilon + P)] = \frac{dE_{\text{cool}}}{dt}, \tag{1c}$$

where ε is the total specific energy ($\varepsilon = \boldsymbol{u}^2/2 + e/\rho$), ρ is the gas density, e is the internal energy density, P is the gas pressure and u is the gas velocity. In order to simulate radiative losses, the parameter dE_{cool}/dt is included, which is the energy loss rate per unit volume from the fluid due to gas and dust cooling.

Spatial reconstruction using a piecewise linear method was performed, while two strong stability Runge-Kutta methods were used for numerical integration, depending on the simulation stability. Several passive scalars are utilised to model wind mixing and dust evolution, which are transported by the fluid. For a given scalar, i, the scalar is advected through the following equation:

$$\rho \frac{dC_i}{dt} = \frac{\partial}{\partial t} (\rho C_i) + \nabla \cdot (C_i \rho \mathbf{u}) = 0, \tag{2}$$

where C_i is the scalar quantity. Passive scalar diffusion is set to 0, hence the scalars are explicitly co-moving with the fluid.

Stellar winds are simulated by modifying the density, ρ_R, momentum, p_R, and energy, E_R in a small region around both stars. Winds flow from this "remap" region at the stars wind terminal velocity, v^∞. Remap zone parameters are calculated with the formulae

$$\rho_R = \frac{\dot{M}}{4\pi r^2 v_\infty}, \tag{3a}$$

$$p_R = \rho_R v_r, \tag{3b}$$

$$E_R = \frac{P_R}{\gamma - 1} + \frac{1}{2} \rho_R v_\infty^2, \tag{3c}$$

where P_R is the cell pressure ($P_R = \rho_R k_B T_w / \mu m_H$), T_w is the wind temperature, μ is the mean molecular mass, m_H is the mass of a hydrogen atom, v_R is the wind velocity as it flows radially from the center of the "remap zone" and r is the distance from the current cell to the centre of the remap zone. This method produces radially outflowing winds from the star with an expected density and velocity.

Line driving and wind acceleration effects are not simulated; instead, winds are instantaneously accelerated to their terminal velocity. Gravitational forces are not calculated as the winds are assumed to be travelling in excess of the system escape velocity.

Athena++ utilises Message Passing Interface (MPI) parallelism. The numerical problem is broken into blocks, which are distributed between processing nodes on a High Performance Compute (HPC) cluster. The block size is variable, but for this simulation a block size of $40 \times 40 \times 10$ cells in XYZ was found to be optimal. Static mesh refinement is used to increase the effective resolution of the simulation. A region around the orbital path of the stars in the simulation is refined to a higher resolution, with gradual de-refinement as a function of distance from this refinement region. This refinement is covered in more detail in Section 3.2.

2.1 Radiative cooling

Cooling is simulated via the removal of thermal energy from a cell at each time-step. A cooling rate, for radiative emission from the stellar wind gas, dE_g/dt, is calculated and integrated using a sub-stepping Euler method. The number of sub-steps is determined by the estimated cooling timescale of the cell. Cooling is calculated via individual lookup tables from each wind. These lookup tables contain the normalised emissivity, $\Lambda_w(T)$ at a logarithmically spaced series of temperatures from 10^4 K to 10^9 K. The cooling rate is determined for a cell by calculating the cell temperature and estimating $\Lambda_w(T)$ using linear interpolation between the nearest emissivity values in the lookup table. The energy loss is then calculated through the equation:

$$\frac{dE_g}{dt} = \left(\frac{\rho_g}{m_H}\right)^2 \Lambda_w(T), \tag{4}$$

where ρ_g is the gas density and m_H is the mass of hydrogen. The lookup table was generated by mixing a series of cooling curves from MEKAL calculation of elemental gasses. These curves were combined based on the elemental abundances in the WC and OB winds. To save calculation time, temperatures between 1×10^4 K $< T \leq 1.1 \times 10^4$ K are set to 1×10^4 K as they are assumed to be either rapidly cooling or a part of the stellar wind outside of the WCR. A minimum temperature of 10^4 K is defined by the simulation, is it is assumed that a radiating post-shock wind will tend to the temperature of the pre-shock wind, $T_{\text{final}} \rightarrow T_{\text{pre-shock}}$.

2.2 Dust model

In order to simulate dust evolution in WR140 a passive scalar dust model that simulates dust growth and destruction is included in the simulation. The dust model operates on passive scalars, and as such

simulates dust that is co-moving with the stellar wind. Two scalars are used to describe dust in a cell, a, the grain radius in microns, and z, the grain dust-to-gas mass ratio

$$z = \frac{\rho_d}{\rho_g}, \tag{5}$$

where ρ_d is the dust density in the cell. A number of assumptions are made in this dust model; for instance, the dust grains in the model are spherical, with a uniform density. Dust grains are assumed to have a single size each grid cell. The number density of grains varies in the simulation volume, however the ratio of grain number density is fixed and constant throughout the simulation. As such, this model does not simulate grain fracturing. Additional mechanisms for dust formation and destruction could also be implemented such as grain-grain agglomeration and photoevaporation. A multi-fluid model with drag force coupling could also be implemented, however this is beyond the scope of this paper.

Dust grows through grain accretion using formulae described by Spitzer (2008) where dust grains grow via low-velocity collisions with surrounding carbon atoms, causing them to accrete onto the surface of the dust grain. Carbon is removed from the gas, reducing the cell gas density, while the corresponding dust density increases. This ensures that mass is preserved in the simulation. Assuming a single average grain size the rate of change in the grain radius in a cell, da/dt, is given by the equation:

$$\frac{da}{dt} = \frac{\xi \rho_C w_C}{4 \rho_{gr}}, \tag{6}$$

where ξ is the grain sticking factor, ρ_C is the carbon density ($\rho_C = X_C \rho_g$), w_C is the Maxwell-Boltzmann RMS velocity for carbon ($w_C = \sqrt{3 k_B T / 12 m_H}$), k_B is the Boltzmann constant and ρ_{gr} is the grain bulk density. The rate of change in the mass of a single grain due to accretion, $dm_{gr,ac}/dt$, is calculated with the formulae:

$$\frac{dm_{gr,acc}}{dt} = 4\pi \rho_{gr} a^2 \frac{da}{dt} = \pi \xi \rho_C w_C a^2, \tag{7}$$

A bulk density approximating that of amorphous carbon grains ($\rho_{gr} = 3.0 \, \text{g cm}^{-3}$) is used for this simulation.

Dust destruction through gas-grain sputtering is calculated using the Draine & Salpeter (1979) prescription. Within a flow of gas number density n_g a dust grain of radius a has a grain lifespan, τ_{gr} of:

$$\tau_{gr} = \frac{a}{\dot{a}} \approx 3 \times 10^6 \frac{a}{n_g} \, \text{yr.} \tag{8}$$

This value is based on an average lifetime of carbon grains in an interstellar shock with a temperature of $1 \times 10^6 \, \text{K} \leq T \leq 3 \times 10^8 \, \text{K}$ (Tielens et al. 1994; Dwek et al. 1996). The rate of change in the mass of a single dust grain due to sputtering, $dm_{gr,sp}/dt$, can then be calculated with a similar formula to the rate of change in grain mass due to accretion:

$$\frac{dm_{gr,sp}}{dt} = -4\pi \frac{\rho_{gr} a^3}{\tau_d} = -4\pi \frac{\rho_{gr} n_g a^2}{3 \times 10^6} \tag{9}$$

The overall change in dust density is then calculated through the equation:

$$\frac{d\rho_d}{dt} = \left(\frac{dm_{gr,acc}}{dt} + \frac{dm_{gr,sp}}{dt} \right) n_d, \tag{10}$$

where n_d is the dust grain number density.

Cooling via emission of photons from dust grains is also included in this model. The rate of cooling is calculated using the uncharged grain case of the prescription described in Dwek & Werner (1981). Grains are collisionally excited by collisions with ions and electrons, causing them to radiate. Similarly to the gas/plasma emission model used, the emitted photons are not re-adsorbed by the WCR medium, causing energy to be removed from the simulation. This therefore makes the assumption that the WCR is optically thin to far-infrared photons, which is observationally correct (Monnier et al. 2007; Soulain et al. 2018; Callingham et al. 2019). The grain heating rate, H_{coll}, in erg s^{-1} for a dust grain is calculated with the formulae:

$$H = 1.26 \times 10^{-19} \frac{n_g}{A^{1/2}} a^2 (\mu m) T^{3/2} h(a,T), \tag{11}$$

where n_g is the gas number density, A is the mass of the incident particle in AMU, $a(\mu m)$ is the grain radius in microns, T is the temperature of the ambient gas, and $h(a,T)$ is the effective grain heating factor. Individual heating rates for hydrogen, helium, carbon, nitrogen and oxygen are calculated, in order to calculate the total ion collisional heating, H_{coll}:

$$H_{coll} = H_H + H_{He} + H_C + H_N + H_O. \tag{12}$$

The effective grain heating factor for each element is calculated via the equation:

$$h(a,T) = 1 - \left(1 + \frac{E^*}{2 k_B T} \right) e^{-E^*/k_B T}, \tag{13}$$

where E^* is the critical energy required for the particle to penetrate the dust grain (Table 2). The rate of heating due to electron-grain collisions, H_{el}, is similar to Eq. 11. The grain heating factor for electron collisions, h_e, is calculated via an approximation rather than the exact calculation in the case of baryonic matter. h_e is estimated through the following conditions:

$$\begin{aligned} h_e(x^*) &= 1, & x^* &> 4.5, \\ &= 0.37 x^{*0.62}, & x^* &> 1.5, \\ &= 0.27 x^{*1.50}, & &\text{otherwise,} \end{aligned} \tag{14}$$

where $x^* = 2.71 \times 10^8 a^{2/3}(\mu m)/T$. This approximation differs from the integration method by less than 8% while being 3 orders of magnitude faster. Excitation due to grain-grain collisions were not modelled, due to the limitations of the passive scalar model. In order to calculate the change in energy due to dust cooling, we find the radiative emissivity for dust, $\Lambda_d(T,a)$, to be

$$\Lambda(T,a) = \frac{H_{coll} + H_{el}}{n_H}, \tag{15}$$

where n_H is the number density of hydrogen in the gas. The energy loss rate from dust cooling, dE_d/dt, then calculated with the equation:

$$\frac{dE_d}{dt} = n_T n_d \Lambda_d(T,a), \tag{16}$$

and added to the gas/plasma energy loss rate, such that the total energy loss rate is:

$$\frac{dE_{cool}}{dt} = \frac{dE_g}{dt} + \frac{dE_d}{dt}. \tag{17}$$

Particle	E^*
e^-	$23\,a^{2/3}\,(\mu m)$
H	$133\,a\,(\mu m)$
He	$222\,a\,(\mu m)$
C	$665\,a\,(\mu m)$
N	$665\,a\,(\mu m)$
O	$665\,a\,(\mu m)$

Table 2. Grain critical energy, E^*, for a dust grain of a in μm for electrons, e^-, as well as the elements considered for grain cooling. The values for carbon, oxygen and nitrogen are identical.

3 SYSTEM PARAMETERS

We have previously simulated WCd systems in the form of a parameter space exploration, in order to discern which wind and orbital parameters are influential on the dust growth rates *CITE EATSON ET AL. 2022 WHEN PUBLISHED*. It was determined that the primary factors of dust growth in a WCd system were the mass loss rates, $\dot{M}$, and wind terminal velocities, v^∞, for each star, as well as the orbital separation, d_{sep}. In particular, it was found that imbalances between the wind velocity produced Kelvin-Helmholtz (KH) instabilities due to a shear in the winds. Slower winds were found to be more radiative in the post-shock WCR flow, cooling to temperatures suitable for dust formation. This was found to influence the dust growth rate by as much as six orders of magnitude through a factor of four variation of the WR wind terminal velocity. We also found that increasing d_{sep} significantly reduced the dust production rate, due to less intensive shocks as the out-flowing winds became less dense with distance. In the case of WCd systems with eccentric orbits, the separation distance can vary significantly. In the case of WR140, d_{sep} varies by a factor of 18 from apastron to periastron. This is hypothesised to be the primary cause of dust production variability within episodic systems. The pre-shock velocity can also vary somewhat due to radiative inhibition and orbital motion.

In order to understand the structure and dynamics of the CWB system we must define some important parameters, such as the wind momentum ratio, η, which is defined as:

$$\eta = \frac{\dot{M}_{OB}\,v^\infty_{OB}}{\dot{M}_{WR}\,v^\infty_{WR}}. \tag{18}$$

As η decreases we find that the wind becomes more imbalanced. In the case of WR+OB CWB systems we find that the WR stars wind typically dominates the WCR. Assuming that there is no radiative inhibition (Stevens & Pollock 1994) or radiative braking (Gayley et al. 1997), we can approximate the WCR to a conical region with an opening angle:

$$\theta_c \simeq 2.1\left(1 - \frac{\eta^{2/5}}{4}\right)\eta^{-1/3} \quad \text{for } 10^{-4} \leq \eta \leq 1, \tag{19}$$

to a relatively high degree of accuracy (Eichler & Usov 1993). Another important value for determining the nature of the WCR is the cooling parameter, χ, which is the ratio of the time taken for the shocked wind to completely cool to the time taken for the wind to escape the shocked region:

$$\chi = \frac{t_{cool}}{t_{esc}} \approx \frac{v_8^4 d_{12}}{\dot{M}_{-7}}, \tag{20}$$

where v_8 is the wind terminal velocity in units of $10^8\,\mathrm{cm\,s^{-1}}$, d_{12} is the separation distance in units of 10^{12} cm and $\dot{M}_{-7}$ is the wind

Parameter	Value	Citation
M_{WR}	$10.31\,\mathrm{M_\odot}$	Thomas et al. (2021)
M_{OB}	$29.27\,\mathrm{M_\odot}$	Thomas et al. (2021)
P	7.926 yr	Thomas et al. (2021)
e	0.8993	Thomas et al. (2021)
$\dot{M}_{WR}$	$5.6 \times 10^{-5}\,\mathrm{M_\odot\,yr^{-1}}$	Williams et al. (1990)
$\dot{M}_{OB}$	$1.6 \times 10^{-6}\,\mathrm{M_\odot\,yr^{-1}}$	Williams et al. (1990)
v^∞_{WR}	$2.86 \times 10^3\,\mathrm{km\,s^{-1}}$	Williams et al. (1990)
v^∞_{OB}	$3.20 \times 10^3\,\mathrm{km\,s^{-1}}$	Williams et al. (1990)
η	0.031	Calculated
χ_{min}	2.69	Calculated

Table 3. The system parameters for the WR140 system as used in this paper. References for each parameter are provided.

Element	Solar	WC
X_H	0.705	0.000
X_{He}	0.275	0.546
X_C	0.003	0.400
X_N	0.001	0.000
X_O	0.010	0.050

Table 4. Abundances used for the OB and WR stars being simulated. Other elements are assumed to be trace when calculating dust emission (Williams et al. 2015).

mass loss rate in units of $10^{-7}\,\mathrm{M_\odot\,yr^{-1}}$ (Stevens et al. 1992). As χ decreases, the structure of the WCR becomes more influenced by cooling. If $\chi < 1$, the WCR is completely dominated by radiative cooling, while if $\chi \gg 1$, the WCR behaves adiabatically. If the WCR is highly radiative the total compression can be significantly greater than the adiabatic limit of 4 for a $\gamma = 5/3$ gas, which facilitates dust production. Finally, we define a maximum dust production rate of the system, $\dot{M}_{d,max}$, assuming a 100% conversion rate of WR wind in the WCR into dust. The fraction of the WR wind that is passed through the WCR is given by the equation:

$$f_{WR} = \frac{1 - \cos(\theta_{WR})}{2}, \tag{21}$$

where θ_{WR} is the opening angle of the WR shock front ($\theta_{WR} \approx 2\tan^{-1}(\eta^{1/3}) + \pi/9$, see Pittard & Dawson (2018)). $\dot{M}_{d,max}$ is then calculated with the formulae:

$$\dot{M}_{d,max} = \dot{M}_{WR}X_{C,WR}f_{WR}, \tag{22}$$

where $X_{C,WR}$ is the carbon mass fraction in the WR star.

3.1 WR140 parameters

WR140 was simulated in this paper as it is an archetypical example of an episodic WCd system. The system has an extremely eccentric orbit, which significantly affects the cooling parameter as the orbit progresses, and is also observed in detail. Both stellar winds are expected to be accelerated to close to their terminal wind velocities before they collide (Lamers & Cassinelli 1999).

Recent improved estimations of the orbital parameters of WR140 by Thomas et al. (2021) were used to calculate the orbit for these simulations, while the mass loss rate, and the wind terminal velocity were taken from Williams et al. (1990) (see Table 3). A typical wind composition for WC stars was assumed for the Wolf-Rayet star, while a solar abundance was assumed for the OB star (Table 4).
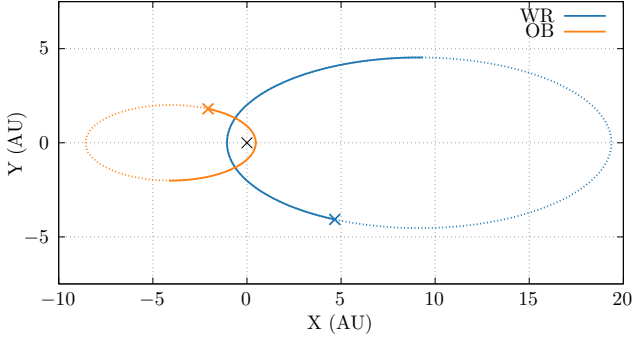
Figure 1. Orbital trajectories of the WC7 and O5 stars in WR140. The solid lines represent the orbital phase being simulated, corresponding to $0.95 \leq \Phi \leq 1.10$, while the dashed lines represent the full orbital trajectory. The starting position for each star and the orbital barycentre at (0,0) are annotated.
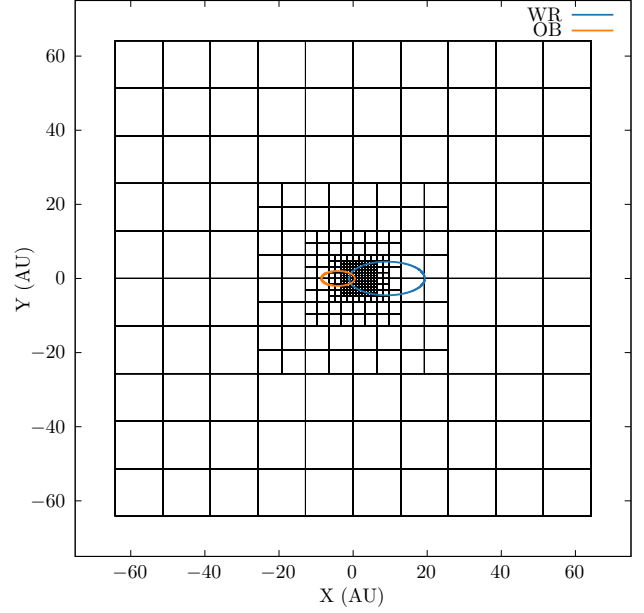

Figure 2. Numerical grid of the WR140 system simulation at $z = 0$. Static mesh refinement was used to increase the resolution around the orbital path from $0.95 \leq \Phi \leq 1.10$. The orbital path of both stars are overlaid onto this numerical grid. The stars are typically in the 3rd or 4th level.

3.2 Simulation parameters

A domain of $128 \times 128 \times 16$ AU was used for this simulation, with a coarse (0th level) grid resolution of $400 \times 400 \times 50$ cells in the XYZ domain. The simulation has 4 refinement levels, corresponding to an effective resolution of $6400 \times 6400 \times 800$ cells and a cell size of 0.02^3 AU^3. At periastron passage this results in ~ 80 cells between the stars, which was found to be enough to adequately resolve the WCR. This simulation has an XYZ aspect ratio of 8:8:1 in order to reduce processing time, as the bulk of dust formation was expected to occur a short distance from the WCR. A section of the systems orbit, corresponding to an orbital phase of $0.95 \leq \Phi \leq 1.10$ was simulated (Fig. 1). This represents 1.2 year section of the systems orbit, and is the orbital period where much of the dust forms - prior to and shortly after periastron passage (Crowther 2003). Fig. 2 shows the orbit overlaid onto the statically refined numerical grid. The area of maximum refinement is around the orbital paths of the stars from $0.94 \leq \Phi \leq 1.11$, in order to ensure that the stars and the apex of the WCR are maximally refined. The simulation was run with two different numerical integrators, a 3rd order accurate Runge-Kutta integrator, `rk3`, and a 4th order accurate, 5-stage, 3 storage register strong stability preserving Runge-Kutta integrator, `ssprk5_4` (Ruuth & Spiteri 2005). The `ssprk5_4` integrator was found to be approximately 60% slower, but markedly more stable. Prior to periastron passage the `rk3` integrator was used for its speed, but increasing numerical instability as the stars grew closer resulted in this proving untenable, and it was switched to `ssprk5_4` for the remainder of the simulation.

During periastron passage the average time-step was found to reduce by an order of magnitude, resulting in a corresponding increase to simulation time. At the most numerically complex portion of the simulation, a Courant number of $C = 0.04$ had to be used instead of the initial value of $C = 0.15$, in order to preserve numerical stability. As the simulation moved past periastron the Courant number was increased every 24 hours of wall time, until C returned to the initial value. The simulation was conducted on the ARC4 HPC cluster at the University of Leeds with 128 cores. The code was compiled using the Intel `ICPC` compiler using `AVX512` optimisations and the Intel MPI library.

3.3 Data collection

Simulation data was exported as HDF5 files at regular time intervals. 3D meshes were collected every increment of $\delta\Phi = 1.5 \times 10^{-3}$, while 2D slices in the XY plane were collected every increment of $\delta\Phi = 1.5 \times 10^{-4}$. These HDF5 files contain the primitive variables of the simulation: gas density, ρ, gas pressure, P, and wind velocity components, v_x, v_y and v_z. These variables were then used to derive other variables such as temperature and energy. The scalars governing the dust properties were also stored for each cell: the dust-to-gas mass ratio, z, and the dust grain radius, a. The wind "colour", the proportion of gas from each star, was also stored. A value of 1.0 indicates a pure WR wind while 0.0 indicates a pure OB wind. The volume-weighted totals of all parameters of interest were also collected, such as the average values for z, a and the dust production rate within the WCR, $\dot{M}_d$. To calculate $\dot{M}_d$, a cell must be identified as being within the WCR. This was performed by comparing the cell density to the predicted density of a single wind with the wind parameters of the WC star in the system. Any cell with a density higher than a certain threshold value was flagged as being within the WCR. The single-wind density, ρ_{SW}, was calculated using the equation:

$$\rho_{SW} = \frac{\dot{M}_{SW}}{4\pi r^2 v_{SW}^{\infty}}, \tag{23}$$

where r is the distance from the barycentre. This threshold value was set to $\rho_{thres} = 1.25\rho_{SW}$, which was found to accurately identify the WCR through thorough prior testing.

Parameter	Mean	Maximum
$\dot{M}_d$ ($M_\odot$ yr^{-1})	7.68×10^{-8}	1.24×10^{-6}
$\bar{a}$ (μm)	1.32×10^{-2}	1.44×10^{-2}
$\bar{z}$	3.98×10^{-4}	3.32×10^{-3}

Table 5. Advected scalar yields from the WR140 simulation.
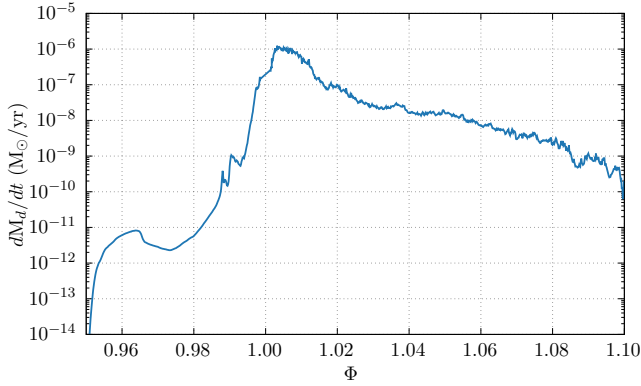
Figure 3. A graph of the dust production rate in the WCR over the orbital phase $0.95 \leq \Phi \leq 1.10$. The dust production rate sharply increases as the stars pass their closest approach. Afterwards, the dust production rate begins to falter and slow, due to weaker wind collision effects via the separation distance and radial velocity.
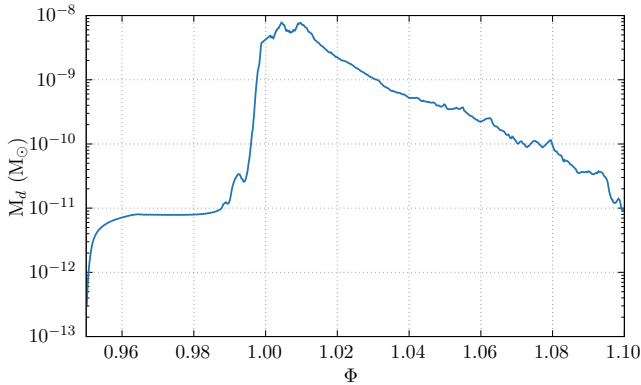
Figure 4. A graph of the overall dust mass in the simulation of WR140 over the orbital phase $0.95 \leq \Phi \leq 1.10$. The amount of dust quickly reduces after periastron due to a decreased dust growth rate (Fig. 3), as well as dust advecting off the numerical grid.

4 RESULTS

Dust growth was found to be consistent with previous uses of this particular dust model. Dust production rates were found to be sensible, and below the theoretical maximum dust formation rate, $\dot{M}_{d,max} \approx 4.8 \times 10^{-6} M_\odot$ yr^{-1}. After an initial advection period lasting until $\Phi \approx 0.96$, the dust production rate rapidly increased as the stars approached periastron passage, peaking at $\Phi \sim 1.01$ (Fig. 3). This maximum dust production rate of $1.24 \times 10^{-6} M_\odot$ yr^{-1} is sensible, but incredibly prodigious. We find peak conversion efficiency of gas into dust of $\sim 26\%$ in the WCR compared to the theoretical maximum dust production rate described in Eq. 22, as well as a total conversion efficiency of $\sim 2.2\%$ throughout the entire system (assuming a total mass loss rate of $5.76 \times 10^{-5} M_\odot$ yr^{-1}). The majority of

dust production ($\gtrsim 90\%$) is produced within the WCR. After reaching this maximum value, the dust production rate steadily decreases as the stars recede from each other. This is reflected in the overall dust mass of the simulation (Fig. 4), as well as in infrared observations of WR140, where the infrared emission from dust formation rapidly reaches a maximum value after periastron passage, and slowly relaxes to a minimum value. This asymmetry in the time-dependent change in infrared luminosity implies the existence of several factors for suppression and encouragement of dust formation than just the change in orbital separation distance. It should be noted that due to the small size of the simulation, the dust mass in the system will reduce quickly, as dust advects off the numerical grid.

The evolution of dust in this system would result in the formation of an expanding cloud of dust every time the system passes periastron, with no contiguous spiral pattern forming, due to the lengthy "dormant" period occurring shortly after periastron passage. This is consistent with observations of WR140, where these disconnected clouds are observed (Williams et al. 2009). We find an average dust production rate of $\dot{M}_d = 7.68 \times 10^{-8} M_\odot$ yr^{-1} over the entire simulation, and a change in the dust production rate by approximately five orders of magnitude over the course of the simulation. This fits our understanding of an episodic dust forming WCd system, with an extremely clear "active" period followed by a slow tapering off of dust production as the system approaches the "dormant" period. We can compare our results to the estimated dust yields from Lau et al. (2020), which found an average dust production rate of $\dot{M}_d = 8.11 \times 10^{-10} M_\odot$ yr^{-1} throughout an entire orbit of WR140. Our value for the dust-to-gas mass ratio within the system appears to be sensible, while our average dust production rate is significantly higher. This is due to the limited temporal sample of the simulation. We would find a significantly lower average dust production rate over the course of a full orbit due to more sampling of the system over the "dormant" period.

4.1 Instabilities

As can be seen in Fig. 5, after periastron passage the post-shock WCR region transitions from a smooth adiabatic wind to a highly radiative wind dominated by instabilities. As the WCR becomes increasingly radiative, dust growth drastically increases, with the bulk of dust production occurring within the high density regions produced by these instabilities. However these clumpy pockets of gas do not exhibit significant dust growth beyond ~ 20 AU from the simulation barycentre, with concentrations of dust remaining approximately constant (Fig. 6). By the end of the simulation at $\Phi = 1.10$, the WCR is still somewhat dominated by instabilities, with an elevated dust production rate even though the cooling parameter has increased significantly to $\chi = 19.7$, which would normally imply adiabatic behaviour. Whilst the dust production rate has reduced significantly, there is still a significantly greater growth rate than at the start of the simulation (after advection). Clearly the transition from radiative back to adiabatic behaviour has a degree of latency, with instabilities still driving the structure of the WCR long after an adiabatic flow should have re-established. Such behaviour was first reported by Pittard (2009) and leads to hysteresis in the x-ray emission (Pittard & Parkin 2010). This is the key physics responsible for the asymmetric dust growth rate about periastron. It seems that once instabilities form in the WCR, they are somewhat difficult to stop - and cause oblique shocks, with lower post-shock temperature and ultimately stronger cooling than expected. The amount of wind being mixed in the WCR also significantly increases after periastron passage, which would be conducive to the formation of complex
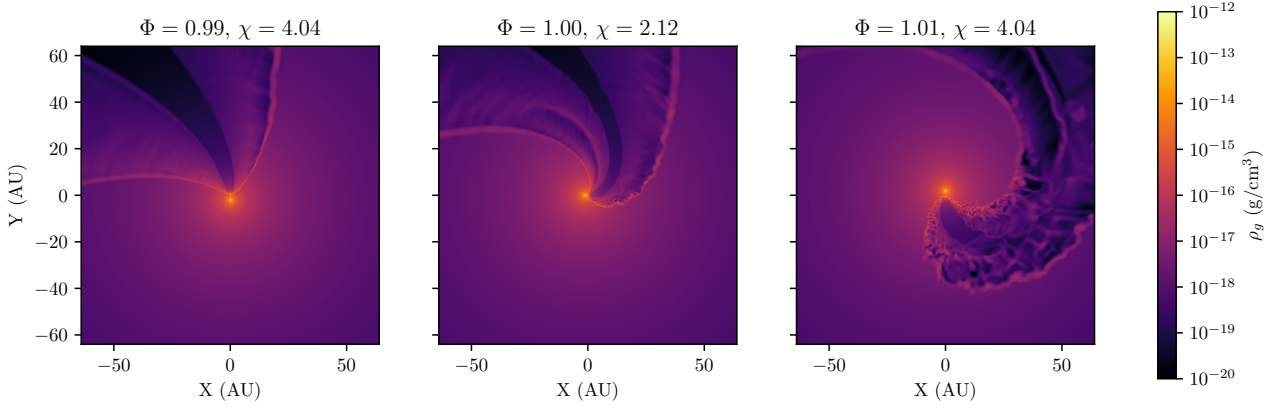
Figure 5. Gas density in a simulation of the WR140 system shortly before, during, and after periastron. The value of χ is calculated using Eq. 20 and the WR wind parameter is noted in each panel. The simulation becomes dominated by instabilities after periastron. These instabilities persist despite the system behaving adiabatically at $\Phi = 0.99$, when the orbital separation distance is identical. This suggests that the radiative behaviour of the post-shock WCR is due to other factors, in addition to $d_{\rm sep}$.
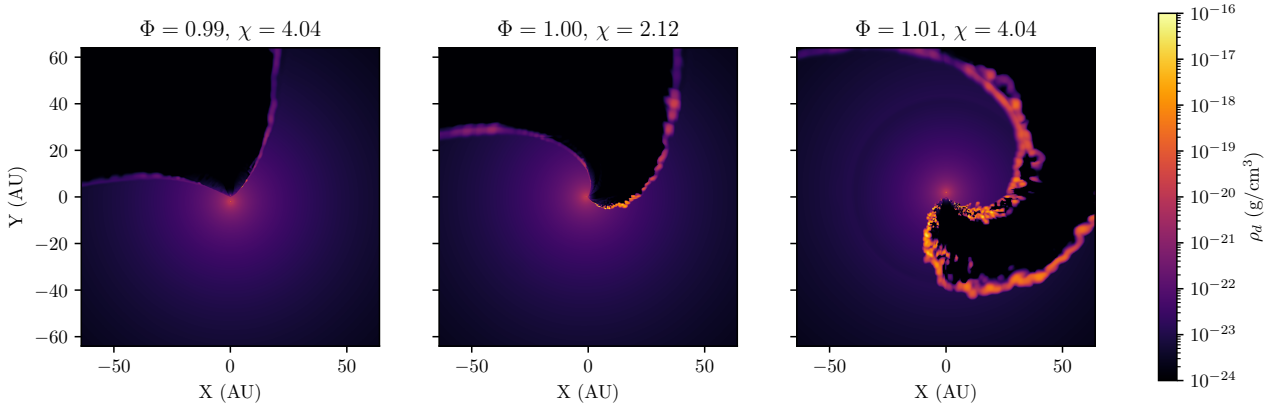
Figure 6. Dust density in a simulation of the WR140 system shortly before, during, and after periastron. Dust growth occurs as a direct result of the formation of cold, dense gas in the post-shock WCR.
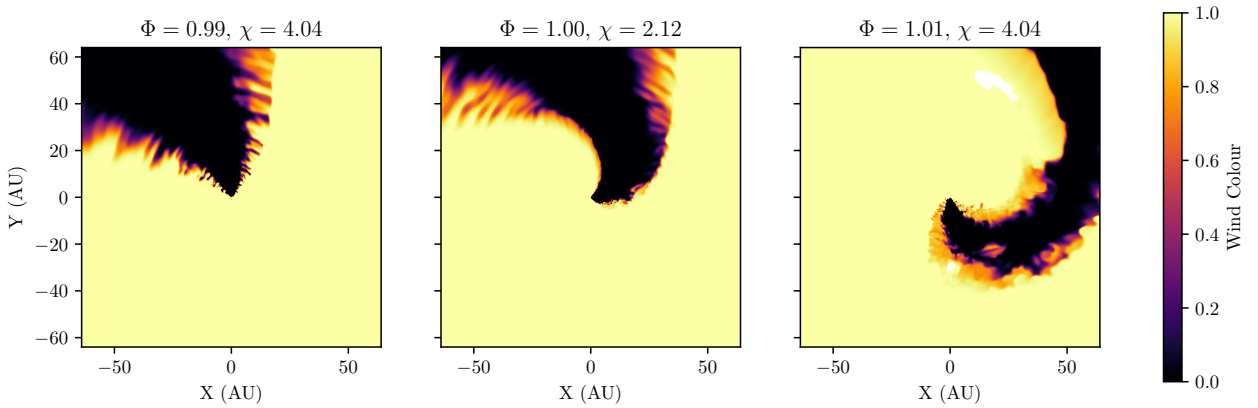

Figure 7. Wind "colour" in a simulation of the WR140 system shortly before, during, and after periastron. A colour of 1 represents a pure WR wind and a colour of 0 represents a pure OB wind. We find that the wind undergoes more mixing during and after periastron.

organic molecules on the surface of the dust grains (Fig. 7). Whilst this is beyond the scope of the current work, evolution of dust grains from WCd systems on longer time and length scales would be an enlightening avenue of research.

4.2 Influence of varying wind velocity on dust production

As we have previously discussed, varying the wind terminal velocity for both stars in a simulation can result in significant changes in the dust production rate. This is theorised to be due to the increased cooling in the WCR caused by slower winds, as well as through KH instabilities driven by a wind velocity shear (if the wind terminal velocities are significantly different, see Stevens et al. (1992)). Previous work on this subject considered systems with circular orbits *«CITE EATSON ET AL. 2022 WHEN PUBLISHED»*, where the pre-shock velocities are constant over the orbit of the system. However, in the case of a system with an eccentric orbit (such as WR140), the outflow velocity for each wind, as well as their ratio, can markedly vary over the systems orbit. As the stars approach periastron, the radial velocity, v_r, for each star rapidly changes from a maximum value to a minimum, as the stars approach and then swing past one another (Fig. 8). This causes a rapid change in the pre-shock velocity for both winds. This then influences the amount of radiative cooling in the post-shock wind, suppressing radiative cooling pre-periastron and inciting it post-periastron; leading to changes in the dust production rate. While the change in wind velocity is relatively small (with the wind velocity varying by as much as 6% over the course of an orbit) it still impacts the cooling of the system, and can vary χ by as much as a factor of 1.26 in the case of WR140.

The rate of dust production is also affected by the presence of a large wind velocity ratio, Υ, where:

$$\Upsilon = v_{OB}/v_{WR}. \tag{24}$$

As the mass of each star is different, the change in radial velocity differs for each star, causing a variability in the velocity ratio and therefore velocity shear. Previous research with dust models suggests that a strong velocity shear drives an increased dust production rate. We find that the maximum velocity shear occurs at $\Phi = 1.01$ (Fig. 8), around the same time where the dust growth rate is at a maximum; this is consistent with our previous work. This change in velocity shear may therefore be another factor behind the increased dust growth of WR140 post-periastron.

We also note that in reality there could be significant change in the pre-shock velocity of the O wind due to the WCR encroaching into the acceleration region during periastron (Sugawara et al. 2015).

5 SUMMARY

Despite only simulating a limited section of the orbit of WR140, we have made a number of insights into the behaviour of the system. We find a significant degree of change in the dust production rate as a direct consequence of the changing orbital separation of the system. This is related to the change in the behaviour of the post-shock WCR wind, which goes from a smooth adiabatic wind to a clumpy, high density wind dominated by instabilities ideal for dust growth. It is particularly interesting to note that the system does not revert to behaving adiabatically as quickly as expected. This suggests that the post-shock WCR condition of the system is dependent on additional factors, instead of being solely due to d_{sep}. One of the factors on this delayed return to the adiabatic state is potentially due to the
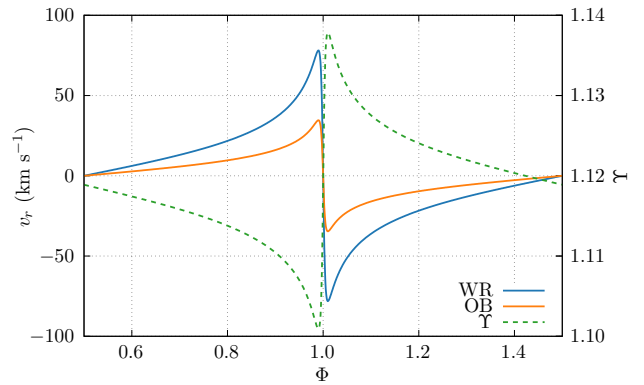
Figure 8. Radial velocity as a function of the orbital phase for the WR and OB stars in the WR140 system relative to the barycentre. As periastron passage occurs, the sudden inversion from approaching to receding can alter pre-shock the wind velocity of the WR star by as much as 160 km s^{-1}. Whilst this is $\sim$ 6% of the WR wind velocity, it can significantly increase dust production when the stars recede from each other. The velocity shear, $\Gamma = v_{OB}/v_{WR}$, also sharply increases during periastron passage, peaking at the point of maximum dust production.

orbital motion of the stars themselves. As the stars approach each other at periastron, the radial velocity of the stars adds velocity to the wind beyond the outflow velocity, resulting in higher wind collision velocities, which encourages adiabatic behaviour in the post-shock flow. The inverse is true as the stars recede from one another: the effective wind velocity for both stars is reduced, which encourages cooling and the formation of instabilities in the WCR. Furthermore, an increased wind velocity ratio occurs after periastron due to the orbital dynamics which can drive KH instabilities.

REFERENCES

Callingham J. R., Tuthill P. G., Pope B. J. S., Williams P. M., Crowther P. A., Edwards M., Norris B., Kedziora-Chudczer L., 2019, Nat. Astron., 3, 82
Crowther P. A., 2003, Astrophys. Space Sci., 285, 677
Draine B. T., Salpeter E. E., 1979, ApJ, 231, 77
Dwek E., Werner M. W., 1981, ApJ, 248, 138
Dwek E., Foster S. M., Vancura O., 1996, ApJ, 457, 244
Eichler D., Usov V., 1993, ApJ, 402, 271
Gayley K. G., Owocki S. P., Cranmer S. R., 1997, ApJ, 475, 786
Hendrix T., Keppens R., van Marle A. J., Camps P., Baes M., Meliani Z., 2016, MNRAS, 460, 3975
Lamers H. J., Cassinelli J. P., 1999, Introduction to Stellar Winds. Cambridge University Press
Lau R. M., Eldridge J. J., Hankins M. J., Lamberts A., Sakon I., Williams P. M., 2020, ApJ, 898, 74
Monnier J. D., Tuthill P. G., Danchi W. C., 1999, ApJ, 525, L97
Monnier J. D., Tuthill P. G., Danchi W. C., Murphy N., Harries T. J., 2007, ApJ, 655, 1033
Pittard J. M., 2009, Monthly Notices of the Royal Astronomical Society, 396, 1743

Pittard J. M., Dawson B., 2018, MNRAS, 477, 5640

Pittard J. M., Parkin E. R., 2010, Monthly Notices of the Royal Astronomical Society, 403, 1657

Prilutskii O. F., Usov V. V., 1976, Soviet astron., 20, 2

Rosslowe C. K., Crowther P. A., 2015, MNRAS, 447, 2322

Ruuth S. J., Spiteri R. J., 2005, SIAM Journal on Numerical Analysis, 42, 974

Soulain A., et al., 2018, A&A, 618, A108

Spitzer L., 2008, Physical Processes in the Interstellar Medium. John Wiley & Sons

Stevens I. R., Pollock A. M. T., 1994, MNRAS, 269, 226

Stevens I. R., Blondin J. M., Pollock A. M. T., 1992, ApJ, 386, 265

Stone J. M., Tomida K., White C. J., Felker K. G., 2020, ApJS, 249, 4

Sugawara Y., et al., 2015, Publications of the Astronomical Society of Japan, 67, 121

Thomas J. D., et al., 2021, MNRAS, 504, 5221

Tielens A. G. G. M., McKee C. F., Seab C. G., Hollenbach D. J., 1994, ApJ, 431, 321

Tuthill P. G., Monnier J. D., Danchi W. C., 1999, Nature, 398, 487

Williams P. M., van der Hucht K. A., Thé P. S., 1987, A&A, 182, 91

Williams P. M., van der Hucht K. A., Pollock A. M. T., 1990, MNRAS, 243, 662

Williams P. M., et al., 2009, MNRAS, 395, 1749

Williams P. M., Crowther P. A., van der Hucht K. A., 2015, MNRAS, 449, 1834

This paper has been typeset from a TeX/LaTeX file prepared by the author.